LRRC23 loss-of-function impairs radial spoke 3 head assembly and causes defective sperm motility underlying male infertility

Jae Yeon Hwang[a,1,2], Pengxin Chai[b,1], Shoaib Nawaz[c,1,3], Jungmin Choi[d,e], Francesc Lopez-Giraldez[f], Shabir Hussain[g,4], Kaya Bilguvar[d,f], Shrikant Mane[f], Richard P. Lifton[h], Wasim Ahmad[c,f], Kai Zhang[b], Jean-Ju Chung[a,i,*]

[a]Department of Cellular and Molecular Physiology, Yale School of Medicine, Yale University, New Haven, CT, 06510 [b]Department of Molecular Biophysics and Biochemistry, Yale School of Medicine, Yale University, New Haven, CT, 06510 [c]Department of Biotechnology, Faculty of Biological Sciences, Quaid-i-Azam University, 45320, Islamabad, Pakistan [d]Department of Genetics, Yale School of Medicine, Yale University, New Haven, CT, 06510 [e]Department of Biomedical Sciences, Korea University College of Medicine, Seoul, South Korea, 02841 [f]Yale Center for Genome Analysis, Yale University, West Haven, CT, 06516 [g]Department of Biochemistry, Faculty of Biological Sciences, Quaid-i-Azam University, 45320, Islamabad, Pakistan [h]Laboratory of Human Genetics and Genomics, The Rockefeller University, New York, NY, 10065 [i]Department of Obstetrics, Gynecology and Reproductive Sciences, Yale School of Medicine, Yale University, New Haven, CT, 06510

*Correspondence author: Jean-Ju Chung

Email: jean-ju.chung@yale.edu

[1]The authors contribute equally.

[2]Present address, Department of Molecular Biology, Pusan National University, Pusan, South Korea, 46241 [3]Present address, Department of Human Genetics, Sidra Medicine, Doha, Qatar [4]Present address, Clinical and Molecular Metabolism (CAMM) Program, Faculty of Medicine, University of Helsinki, Helsinki, Finland

Author Contributions: J.H., K.Z. and J-J.C. designed the research; J.H., P.C., S.N. and S.H. performed research; J.C., F.L-G., K.B., and S.M. analyzed data; P.C. and K.Z. performed cryo-ET and structural analysis; J-J.C., W.A., K.Z. and R.P.L provided resources. J.H., P.C., S.N., K.Z. and J-J.C. wrote the paper.

Competing Interest Statement: The authors declare no competing interest.

Abstract

Radial spokes (RSs) are T-shaped multiprotein complexes in the 9+2 axoneme of motile cilia and flagella that couple the central pair to the peripheral doublet microtubules. RS1, RS2, and RS3 are repeated along the outer microtubule of the axoneme and modulate the activity of dynein, thus ciliary and flagella movement. RS substructures are distinct in spermatozoa from other cells harboring motile cilia in mammals. However, the molecular components of the cell-type specific RS substructures remain largely unknown. Here, we report a leucine-rich repeat-containing protein, LRRC23, is a RS head component indispensable for the RS3 head assembly and flagellar movement in human and mouse sperm. From a Pakistani consanguineous family with infertile males due to reduced sperm motility, we identified a splice site variant of LRRC23 that leads to truncate LRRC23 at the C-terminus. In mutant mouse model mimicking the identified variant, the truncated LRRC23 protein is produced in testis but fails to localize in the mature sperm tail, causing severe sperm motility defects and male infertility. Purified recombinant human LRRC23 does not interacts with RS stalk proteins, but with a head protein, RSPH9, which is abolished by the C-terminus truncation of LRRC23. Cryo-electron tomography and sub-tomogram averaging unambiguously visualized that the RS3 head and sperm-specific RS2-RS3 bridge structure is missing in the LRRC23 mutant sperm. Our study provides new insights into RS3 structure and function in mammalian sperm flagella as well as molecular pathogenicity of *LRRC23* underlying reduced sperm motility in infertile human males.

Introduction

Motile cilia and flagella are evolutionarily conserved organelles essential for cellular motility (1, 2). The core of motile cilia and flagella is the '9+2' axoneme, characterized by a scaffold structure composed of nine peripheral microtubule doublets (MTDs) and a central pair of singlet microtubules (CP). Each MTD binds two rows of dyneins, the outer-arm dyneins (OAD) and inner-arm dyneins (IAD), which generate mechanical force required for the ciliary beating via ATP hydrolysis (3, 4). Radial spoke (RS) controls the amplitude of the ciliary and flagellar beat by transmitting mechanochemical signals from the CP to the axonemal dyneins (5, 6). In *Chlamydomonas reinhardtii*, RS mutations paralyze the flagellar movement (7) and the axoneme lacking RS system shows reduced velocity of microtubule sliding by dyneins (8). In human and mouse, mutations in RS components or their absence cause primary ciliary dyskinesia (PCD) and/or male infertility due to the defective ciliary and flagellar beating (9-11). These studies highlight the physiological importance of RS in regulating ciliary and flagellar movement.

A triplet of three RSs (RS1, RS2, and RS3) repeats every 96-nm along the peripheral MTDs and this 96-nm periodicity of RS is well-conserved in cilia and flagella across diverse organisms (6, 12). RS is a multiprotein complex; at least 23 RS components were identified in *C. reinhardtii* (6, 13, 14). These RS components are also crucial for RS organization and function in other ciliated and flagellated organisms (11, 15-17), indicating evolutionarily conserved molecular composition of the RS. However, cryo-electron microscopy (cryo-EM) studies have revealed species- and tissue-specific structural variabilities in RS3. For example, RS3 in most species is a T-shaped axonemal structure that consists of a head and a stalk like those of RS1 and RS2 (18-21) but RS3 in *C. reinhardtii* is a headless and stump-like structure (18). In addition, mammalian sperm flagellar axoneme carries a unique bridge structure between RS2 and RS3 (20), which is not observed from tracheal cilia as well as other flagellated organisms (19, 21). This variability suggests that RS3 is an evolutionarily more divergent structure and conveys species- and/or tissue-specific ciliary and flagellar function. Yet, the overall molecular composition of RS3 and the extent to which RS3 components are species- and/or tissue specific remains largely unknown.

Asthenozoospermia (ASZ) (22) is the male infertility classified by reduced sperm motility. ~80% of

male infertile patients manifest sperm motility defects (23) as infertile male with abnormal sperm morphology and/or reduced sperm count often accompany low motility (24, 25). Recent whole exome sequencing studies identified genetic defects in RS components from idiopathic ASZ patients (10, 26, 27). Mutant analyses using model organisms further elucidated the function of RS components in the flagellar movement and the pathogenic mechanisms (10, 26). Thus, WES combined with functional and structural analyses of mutants, especially in a mouse model, would be a powerful and direct approach to understand mammalian specific RS3 roles including sperm motility regulation and genetic etiologies causing male infertility.

Here, we report a bi-allelic loss-of-function splicing variant in *LRRC23* from ASZ patients in a Pakistani consanguineous family. We generated a mouse model that mimics the human mutation and found that the mutation leads to C-terminal truncated LRRC23 and that the mutant mice phenocopy the impaired sperm motility and male infertility. Using biochemical analyses and structural prediction, we showed that, different from previously known, LRRC23 is not the ortholog of a RS2 stalk protein RSP15 but interacts with a known RS head protein. Finally, we visualized the in-cell structures of RS triplets in intact WT and mutant sperm using cryo-electron tomography (cryo-ET). We observed missing RS3 head and aberrant junction between RS2 and RS3 in the mutant flagellar axoneme, unarguably demonstrating that LRRC23 is a head component of RS3. This study provides molecular pathogenicity of *LRRC23* in RS-associated ASZ and reveals unprecedented structural insights into the RS3 and its implication in normal sperm motility and male fertility in mammals.

Results

A Loss of Function Splice Site Variant Truncating LRRC23 is Identified from a Consanguineous Family with Asthenozoospermia

A consanguineous Pakistani family with infertile males was recruited (**Fig. 1*A***). Both infertile males (IV-1 and IV-2) have failed to have child over 3 years of unprotected sex after marriage (***SI Appendix*, Table S1**). The male infertile patients do not show PCD-related symptoms, abnormal heights, weights, secondary characteristics, nor anatomical defects. They also have normal karyotypes without Y chromosome microdeletion. Although the ejaculated sperm from these infertile males are morphologically normal (**Fig. 1*B***, and ***SI Appendix*, Fig. S1*A***), their progressive motility are lower than WHO standard, diagnosing the patients as asthenozoospermia (ASZ) (***SI Appendix*, Table S1**). To understand the genetic etiology underlying the defective sperm motility, we performed whole exome sequencing (WES) on the proband, IV-1. WES estimated 5.02% inbreeding co-efficiency and the longest homozygous-by-descent segment as 37.5 cM, verifying the consanguineous nature of the recruited family. Among the four identified rare variants (***SI Appendix*, Table S2**), only one homozygous splicing donor site variant (c.621+1G>A) in *LRRC23* (leucin-rich repeat containing protein 23) is co-segregated with the male infertility phenotype (**Fig. 1 *A*, *C*, and *D***). Of note, one infertile female sibling (IV-4) also has the homozygous *LRRC23* variant (IV-4) but this phenotype would not be due to the variant because the mother (III-1) also bears the homozygous allele but were fertile (**Fig. 1*A***). The variant at the splicing donor site of *LRRC23* intron 5 is predicted to prevent splicing out of the intron, which can lead to early termination of protein translation with loss of 136 amino acids at the C-terminus (***SI Appendix*, Fig. S1 *B* and *C***). To verify the splicing defects and generation of mutant protein by the variant, we constructed minigenes to express *LRRC23* ORF spanning partial intron 5 with the normal or variant sequence at the splicing site in 293T cells (**Fig. 1*E***). 293T cells transfected with the construct carrying the variant failed to splice out the intronic region (**Fig. 1*F***) and generated only truncated LRRC23 (***SI Appendix*, Fig. S1*D***). These results suggest the variant is pathogenic and explains the male infertility with defective sperm motility in this family.

C-terminally Truncated LRRC23 Fails to Localize in the Flagella and Causes Defective Sperm Motility

LRRC23 is a radial spoke (RS) component (28). Consistent with the ASZ phenotype in our infertile patients with a new splice mutation in *LRRC23*, genetic ablation of *Lrrc23* in mice causes severe sperm motility defects and male infertility (29). However, how the C-terminus truncation of LRRC23 affects the RS structure and function remains unresolved. To better understand detailed function of LRRC23 and the molecular pathogenicity of the identified variant, we generated *Lrrc23* mutant mice by CRISPR/Cas9 genome editing to mimic the predicted outcome in human patients (***SI Appendix*, Fig. S1 and S2*A***). We targeted two regions, one in intron 5 and the other in intron 7 (***SI Appendix*, Fig. S2*B***) to delete exon 6 and 7 together and express truncated LRRC23 at C-terminus. We established two mouse lines with 4,126 or 4,135 bp deletion (*Lrrc23-4126del* and *Lrrc23-4135del*, respectively) (***SI Appendix*, Fig. S2*C***). Both homozygous *Lrrc23-4126del* and *4135del* mice displayed the identical male infertility and defective sperm motility phenotypes in our initial characterization. In this study, we used *Lrrc23-4126del* line as *Lrrc23-mutant* line unless indicated. We observed that truncated *Lrrc23* mRNA is expressed from the mutant *Lrrc23* allele but the total mRNA level of *Lrrc23* in testis is not different from wildtype (WT) to that in *Lrrc23*$^{\Delta/\Delta}$ males (***SI Appendix*, Fig. S2 *D, E,* and *F***). Sequencing the truncated *Lrrc23* mRNA revealed that the transcript would produce mutant LRRC23 containing 27 non-native amino acids translated from 3' UTR instead of 136 amino acids at the C-terminus (***SI Appendix*, Fig. S2*G***). Despite the comparable *Lrrc23* mRNA levels in WT and *Lrrc23*$^{\Delta/\Delta}$ testis, the truncated LRRC23 is detected only marginally in the microsome fraction of *Lrrc23*$^{\Delta/\Delta}$ testis, different from full-length LRRC23 enriched in the cytosolic fraction of WT testis (**Fig. 2*A*** and ***SI Appendix*, Fig. S3 *A* and *B***). In addition, the mutant LRRC23 is not present in epididymal sperm (**Fig. 2 *B* and *C*** and ***SI Appendix*, Fig. S3 *C, D,* and *E),*** indicating that the C-terminal region is essential for proper LRRC23 transportation to the sperm flagella.

Sperm from *Lrrc23*$^{\Delta/\Delta}$ and *Lrrc23-4135del*$^{\Delta/\Delta}$ males are morphologically normal (**Fig. 2*C*** and ***SI Appendix*, Fig. S3 *E and F***) and the epididymal sperm counts of *Lrrc23*$^{+/\Delta}$ and *Lrrc23*$^{\Delta/\Delta}$ males are not significantly different (**Fig. 2*D***). Despite the normal morphology and sperm counts, *Lrrc23*$^{\Delta/\Delta}$ males are 100% infertile (**Fig. 2 *E* and *F***). To further understand how the homozygous *Lrrc23* mutation causes male infertility, we performed Computer Assisted Semen Analysis (CASA). *Lrrc23*$^{\Delta/\Delta}$ sperm motility parameters are significantly altered compared to *Lrrc23*$^{+/\Delta}$ sperm (***SI Appendix*, Fig. S3*G***). *Lrrc23*$^{\Delta/\Delta}$ sperm cannot swim efficiently under viscous conditions that mimic the environment in female reproductive tract (**Fig. 2*G*** and **Movie S1**), and their flagella just vibrate but do not beat normally (**Fig. 2*H*** and ***SI Appendix*, Fig. S3*H* and Movie S2**). In addition, inducing capacitation did not rescue any observed motility defect of *Lrrc23*$^{\Delta/\Delta}$ sperm as demonstrated by flagellar waveform analysis, and CASA measurement of curvilinear velocity (VCL), straight line velocity (VSL), and amplitude of lateral head (ALH). These results suggest the C-terminal truncation dysregulates the flagellar localization of the mutant LRRC23, leading to sperm motility defects and male infertility.

C-terminal Truncation of LRRC23 Abolishes its Interaction with Radial Spoke Head

Recent cryo-ET studies revealed that T-shaped RS structures (i.e., head and stalk) are conserved across the species (19, 20) (**Fig. 3*A***). Three RSs (RS1, RS2, and RS3) are repeated in a 96-nm interval along the flagellar axoneme in mammalian sperm, sea urchin sperm, *Trypanosoma brucei*, and even in *C. reinhardtii* with stump-like RS3 without a head structure (**Fig. 3*A***). LRRC23 is a RS protein in chordate axoneme and has been considered especially as the orthologue of RSP15, a RS2 stalk protein in *C. reinhardtii* (14, 29-31) (**Fig. 3*B***). We initially hypothesized the C-terminal truncation of LRRC23 affects the assembly of a RS stalk and/or its incorporation into the RS2. Thus,

we tested the protein-protein interaction of normal (hLRRC23^{WT}) and mutant (hLRRC23^{Mut}) human LRRC23 with known RS stalk (RSPH3, RSPH22) or head (RSHP6A, RSHP9) proteins using RSPH-trap assay (**Fig. 3 *C, D, and E and SI Appendix*, Fig. S4*A***). Purified GST-tagged hLRRC23^{WT} and hLRRC23^{Mut} proteins (**Fig. 3 *C* and *D***) were incubated with a recombinant human RSPH enriched by immunoprecipitation (**Fig. 3*E***). This trap assay demonstrated that hLRRC23^{WT} interacts only with RSPH9, a RS head protein, among the head and stalk RSPH proteins tested (**Fig. 3*F*** and ***SI Appendix*, Fig. S4*B***). Markedly, hLRRC23^{Mut} does not interact with RSPH9, indicating LRRC23 interaction with RS head via its C-terminus. This result also raises the question whether LRRC23 is a head protein of RS, not a stalk protein, a different picture from previous studies. To test this new hypothesis, we performed BLAST search and found *C. reinhardtii* RSP15 (13) has the highest sequence homology to LRRC34, not LRRC23, in *Ciona intestinalis*. Our phylogenetic and pairwise distance comparison analyses also revealed that LRRC34 orthologs are evolutionarily closer to RSP15 orthologs than LRRC23 orthologs (**Fig. 3*G*** and ***SI Appendix*, Fig. S4*C***). Moreover, AlphaFold-predicted structure of human LRRC34, but not that of LRRC23, presents the same structural features as those of RSP15 (i.e., repeated leucin-rich repeat domains and an α-helix motif in-between) (**Fig. 3*H***). *LRRC34* and *LRRC23* share their gene expression patterns among tissues, most abundantly expressed in the tissues known for ciliary and flagellar function such as retina, testis, and fallopian tube (***SI Appendix*, Fig. S4 *D* and *E***). All these results suggest that LRRC34 is a ciliary and flagellar protein and likely the RSP15 orthologue in chordates, and that LRRC23 function is associated with the RS head.

LRRC23 Mutation Disorganizes Radial Spoke 3 in Sperm Flagella

Next, we examined the impact of LRRC23 loss of function by the C-terminal truncation on the subcellular and ultrastructural organization of sperm. We first compared flagellar compartmentalization between *Lrrc23*$^{+/\Delta}$ and *Lrrc23*$^{\Delta/\Delta}$ sperm. Confocal imaging of immunostained sperm by antibodies against various proteins of known localization did not show any difference on the subflagellar localization of axonemal or peri-axonemal proteins (**Fig. 4*A*** and ***SI Appendix*, Fig. S5*A***). The levels of such flagellar proteins are also not significantly different between *Lrrc23*$^{+/\Delta}$ and in *Lrrc23*$^{\Delta/\Delta}$ sperm (***SI Appendix*, Fig. S5 *B* and *C***). Furthermore, transmission electron microscopy (TEM) did not reveal apparent structural abnormalities in *Lrrc23*$^{\Delta/\Delta}$ sperm flagella (**Fig. 4*B*** and ***SI Appendix*, Fig. S5*D***). These results indicate overall subflagellar and ultrastructural organization in *Lrrc23*$^{\Delta/\Delta}$ sperm is preserved despite almost complete loss of sperm motility. Any structural abnormality in *Lrrc23*$^{\Delta/\Delta}$ sperm would be subtle and local in the axoneme, likely in the RS head region, which requires a higher resolution microscope technique.

To determine how the absence of LRRC23 affects sperm structure in more detail, we performed cryo-ET 3D reconstruction to visualize substructural changes of the sperm axoneme (**Fig. 4*C*** and **Movie S3**). The reconstructed tomogram slices revealed striking details of the RS structural difference between WT sperm and *Lrrc23*$^{\Delta/\Delta}$ sperm (**Fig. 4*C***). In WT sperm, the three RSs are repeated with a typical pattern, in which RS1 and RS2 are recognized by an additional EM density between them (barrel structure, 20) followed by RS3 (**Fig. 4*C***, *left*). In *Lrrc23*$^{\Delta/\Delta}$ sperm, EM densities corresponding to RS3 are significantly weaker than those in WT sperm whereas the structural features of RS1 and RS2 are overall kept unaltered from that of WT sperm (**Fig. 4*C***, *right*). These results strongly indicate that the LRRC23 mutation specifically disorganizes RS3 in the sperm axoneme.

LRRC23 Is a Head Component of Radial Spoke 3

To visualize the structural defects of RS3 along the *Lrrc23*$^{\Delta/\Delta}$ sperm axoneme in more detail (**Fig. 4*C***), we performed sub-tomogram averaging (STA) of the axonemal doublets in 96 nm repeat (i.e., the distance that spans a single set of RS1, RS2, and RS3) on both WT and *Lrrc23*$^{\Delta/\Delta}$ spermatozoa

(**Fig. 5** and ***SI Appendix*, Fig. S6**). Remarkably, the resulting 3D maps reveal that the head region of RS3 is entirely missing in *Lrrc23*$^{\Delta/\Delta}$ sperm whereas the heads of RS1 and RS2 are intact (**Fig. 5 *A*** and ***B***). In addition, superimposition of the 3D STA maps demonstrates that the junctional structure between RS2 and RS3–present in mouse and human sperm but not in *C. reinhardtii* nor in *T. brucei* flagellar axoneme–is also specifically abolished in *Lrrc23*$^{\Delta/\Delta}$ sperm (**Fig. 5*C***). By contrast, *Lrrc23*$^{\Delta/\Delta}$ sperm have intact stalk structures of RS3 like those in WT sperm. Consistent with the protein-protein interaction between LRRC23 and the RS head protein RSPH9 using the RSPH-trap approach (**Fig. 3**), these direct structural observations unarguably clarify that LRRC23 is a RS3 head component and the absence of the RS3 head leads to motility defects in *Lrrc23*$^{\Delta/\Delta}$ sperm. These results demonstrate that the C-terminal truncation of LRRC23 prevents the assembly of RS3 head during spermatogenesis, thus preventing functional RS3 complex formation. Taken together, our functional and structural studies using the mouse model recapitulating the human mutation elucidate the molecular pathogenicity of LRRC23 underlying impaired sperm motility and male infertility (**Fig. *5D***)

Discussion

LRRC23 is a Distinct Head Component of Radial Spoke 3

Accumulating evidence on the structural heterogeneity of radial spokes in cilia and flagella suggests that the molecular organization and function of RS3 is distinct from those of RS1 and RS2. For example, the morphology of RS3 head is distinguished from those of RS1 and 2 in mouse motile cilia (32). Moreover, in the tracheal cilia of the PCD patients, RSPH1 or RSPH4 loss-of-function mutation specifically abolished RS1 and RS2 heads, but not RS3 head (19, 33) even though RS3 shares T-shaped structure just like RS1 and RS2 in most eukaryotic motile cilia and flagella (19-21, 34). Despite these findings, the molecular composition of RS3 head remains largely unknown. The current study demonstrates that LRRC23 is a RS3-specific head component. Previous immuno-EM studies showed that LRRC23 is a conserved RS protein in *C. intestinalis* and mouse (18, 29). It is of note that LRRC23 was originally predicted to be the orthologue of RSP15 in *C. reinharditti*, a RS2 stalk protein, due to the presence of leucine-rich repeat domains (13, 14). Yet, we found LRRC23 orthologues are not conserved in *C. reinharditti* in which RS3 is headless and short stump-like, but present in the species where RS3 head structure is preserved, such as *T. thermophila*, sea urchin, and mammals. Instead of LRRC23, our phylogenetic and structural comparison strongly suggests that LRRC34 is likely the RSP15 orthologue in chordate animals (**Fig. 3** and ***SI Appendix*, Fig. S4**) and a previously unappreciated component of RS2 stalk. Identifying a LRRC34 loss-of-function mutation from ciliopathic children further supports that LRRC34 is a RSP component (35). Our wild type-mutant comparison approach using cryo-ET analyses ultimately clarify that LRRC23 is required for assembling the RS3 head structure (**Figs. 4** and **5**), indicating LRRC23 as a RS3 head component. Interestingly, a RS head component, a RS head component, RSPH9, interacts with LRRC23 but the protein level or the localization of RSPH9 is not altered in *Lrrc23*$^{\Delta/\Delta}$ sperm (***SI Appendix*, Fig. S4**), suggesting that RSPH9 is a head component of RS1 and RS2 like in *C. reinhardtii* (13), but not of RS3. Of note is that an independent study reported that LRRC23 is required for flagellar localization of the RS stalk and fibrous sheath components in mature sperm (29). This discrepancy between two studies is likely due to the presence of the truncated LRRC23 in testis in *Lrrc23*$^{\Delta/\Delta}$ males, which might partly allow flagellar localization of other flagellar components during germ cell development. Although the full picture of molecular composition of RS3 head remains to be revealed, our findings demonstrate LRRC23 is a RS3-specific head component. This conclusion is further supported by the presence of LRRC23 in tracheal cilia (29) that lack the RS2-RS3 bridge structure (20).

LRRC23 is required for mammalian sperm-specific bridge structure between RS2 and RS3

In motile cilia and flagella, a set of three RSs is repeated along the axoneme (6, 19, 20, 34). Notably, a recent cryo-ET study revealed additional RS substructures (i.e., a barrel structure at RS1 and a junctional bridge structure between RS2 and RS3) in mammalian sperm flagella (20). These RS

substructures are not present in the axoneme of sea urchin sperm nor of human motile cilia (19), suggesting they confer a unique axonemal movement specific to mammalian sperm flagella. Our cryo-ET and STA analyses visualized the mammalian sperm-specific RS1 barrel and RS2-RS3 bridge structures in WT sperm flagella, consistent with Leung et al (20). Strikingly, in *Lrrc23* mutant sperm, most of the EM density corresponding to the RS2-RS3 bridge structure is missing and/or altered together with that of the RS3 head (**Figs. 4** and **5**). Considering the absence of RS2-RS3 bridge structure in in tracheal cilia (19), LRRC23 also contributes to assemble this sperm-flagellar RS substructure. Thus, we speculate that RS3 and the RS2-RS3 bridge are crucial structural features in developing flagellar movement unique to mammalian sperm such as hyperactivated motility, which is characterized by high-amplitude and asymmetric flagellar bending. As the RS2-RS3 bridge structure is absent in tracheal cilia (19), our study unambiguously demonstrates that LRRC23 is required for assembling this bridge structure specifically in mammalian sperm flagella. If so, LRRC23 may be localized at the junction between RS2-RS3 bridge structure and RS3 head. The detailed molecular components that comprise the RS2-RS3 bridge requires further study. Profiling and comparing LRRC23 interactomes from mammalian motile cilia and sperm flagella could unveil the cell-type specific molecular organization of RS3.

LRRC23 loss of function causes male infertility in mice and human

Loss-of-function mutations in various RS components that are common to motile cilia and sperm flagella were reported to cause PCD and/or male infertility. Loss-of-function mutations of RSPH1 (36, 37), RSPH3 (38), RSPH4A and RSPH9 (39) were identified from PCD patients. Some of the male patients carrying RSPH1 and RSPH3 mutations were infertile (36, 38). RSPH1, RSPH4A, and RSPH9 knockout mouse models recapitulated the PCD phenotypes such as hydrocephalus and impaired mucociliary clearance (40-42). However, there are other RS components in which mutations only cause male infertility in mice and human. For example, WES of infertile males without PCD symptoms identified mutations in CFAP251 (43, 44) and CFAP61 (10, 45). RSPH6 (9), CFAP251 (44), or CFAP61 (10) deficiency also rendered male mice infertile but without gross abnormalities. These phenotypic differences could be due to a different physiological role of the individual RS component between motile cilia and flagella or a distinct repertoire of the RS components that permits functional redundancy. In our study, LRRC23 mutant mice do not have any apparent gross abnormality but display male infertility (**Fig. 2**). This observation is in line with the previous report by Zhang et al in which the authors noted normal tracheal ciliary beat but immotile sperm in the absence of LRRC23 (29). Supportive of these observations, the infertile male patients in the current study do not show PCD symptoms. This phenotype of male infertility without PCD symptoms in both mice and human suggests the mammalian sperm-specific role of LRRC23 in RS structure and function. Physiological implication of LRRC23 and RS3 in motile cilia is unclear but it is likely dispensable for normal ciliary movement probably due to compensatory and/or redundant RS3 proteins specific to cilia. Whether LRRC23 absence would lead to similar structural aberration in RS3 head of motile cilia requires further study. Intriguingly, LRRC23 loss-of-function impairs primarily flagellar motility but morphology only marginally, which is in distinct from other RS components. For example, the absence of RSPH6, CFAP251, or CFAP61 causes male infertility without PCD symptoms but displays multiple morphological abnormalities of the flagella characterized by absent, short, bent, coiled, and irregular flagella (25). By contrast, LRRC23 mutation and absence do not cause either PCD nor MMAF phenotypes in human and mouse, suggesting a distinct physiological significance of LRRC23 in reduced sperm motility.

Materials and Methods

Patients and clinical investigation

This study was approved from the review board of Quaid-i-Azam University, Islamabad, Pakistan (IRB00003532, IRB protocol # QAU-171) and the Yale Center for Mendelian Genomics. A consanguineous family with infertile males was recruited from Pakistan. Informed consent was provided from the consanguineous family members attended in this study. Semen samples were obtained from infertile male members, Papanicolaou-stained and subjected to clinical investigation

according to the guidelines from WHO (22). Venous bloods were collected from the family members for WES analysis, karyotyping, and genomic DNA PCR. See ***SI Appendix, Materials and Methods*** for details.

Whole-Exome Sequencing and Data Analysis

Whole exome sequencing was carried out as described in our previous study (46). Briefly, gDNA from proband (IV-1) was subjected for WES and sequence reads were aligned to reference human genome (GRCh37/hg19) to generate variant using GATK v3.4 (47, 48). Loss of function mutations and deleterious missense mutations were identified and filtering further to exclude false positives. Co-segregation of the candidate damaging variants and male infertility was confirmed by genomic DNA PCR and Sanger sequencing from the attended family members, III-1 and 2, and IV-1, 2, 3, and 4. See ***SI Appendix, Materials and Methods*** for details.

Animals and sample preparation

Mice were cared in accordance with the guidelines approved by Institutional Animal Care and Use Committee (IACUC) for Yale University (#20079). Wildtype C57BL/6 mice were from Charles River Laboratory and *Lrrc23*-mutant mice were generated using CRISPR/Cas9 genome editing in this study. Mouse testis and epididymal sperm cells were obtained from adult males. Testis fractionization and sperm collection were performed as previous studies (49, 50). See ***SI Appendix, Materials and Methods*** for details.

Mammalian Cell culture and transient protein expression

Human embryonic kidney 293T cells (ATTC) were cultured and used to express recombinant protein transiently. See ***SI Appendix, Materials and Methods*** for details.

RNA extraction, cDNA synthesis, and PCR

Total RNA was extracted from transfected 293T cells and mouse testes and subjected to cDNA synthesis. Synthesized cDNA samples were used for endpoint PCR and quantitative PCR. See ***SI Appendix, Materials and Methods*** for details.

Protein extraction, solubilization, and immunoblotting

Proteins were extracted from fractionized testis samples, epididymal sperm, and transfected 293T cells as previous studies (50). Transfected 293T cells were also solubilized for trap assay. Extracted proteins were denatured and subjected to SDS-PAGE and immunoblotting. See ***SI Appendix, Materials and Methods*** for details.

Molecular cloning

cDNA clones of Human *LRRC23* (HG24717-UT; SinoBiological) human *RSPH3*, *RSPH6A*, and *RSPH9* (616166, 5270908, and 5296237, respectively; Horizon Discovery), and *RSPH22* (OHu31347; GenScript) were purchased. cDNA clones were subcloned into *phCMV3* or *pGEX-6P2* vector to generate mammalian or bacterial expression constructs using Q5 Hot Start High-Fidelity 2X Master Mix (NEB) and NEBuilder HiFi DNA Assembly Kit (NEB). See ***SI Appendix, Materials and Methods*** for details.

Recombinant protein purification

Bacterial expression constructs were transformed to BL21-CodonPlus(DE3)-RIL competent cells (Agilent Technologies) and treated with 1 mM IPTG to express recombinant $LRRC23^{WT}$ and $LRRC23^{Mut}$. The cultivates were solubilized and recombinant proteins were purified using glutathione resin. See ***SI Appendix, Materials and Methods*** for details.

Modified trap assay
293T cells to express RSPH proteins were solubilized and enriched using Surebeads™ Protein A Magnetic Bead (Bio-rad) conjugated with rabbit monoclonal DYKDDDDK antibody. Enriched RSPH proteins were incubated with purified recombinant $LRRC23^{WT}$ and $LRRC23^{Mut}$ and subjected to immunoblotting. See ***SI Appendix, Materials and Methods*** for details.

Sperm fluorescence staining
Fluorescence staining of epididymal sperm cells were performed as previously (46, 50). Briefly, swim-out sperm were washed with PBS and attached on the glass coverslips. The coverslips were fixed, permeablized, and blocked. The coverslips were serially incubated with primary and secondary antibodies followed by mounting. Fluorescence-conjugated PNA was used to observe sperm acrosome. Mounted coverslips were imaged using Zeiss LSM710 LSM Elyra P1 (Carl Zeiss). See details in ***SI Appendix, Materials and Methods***.

Mating test
Adult heterozygous and homozygous *Lrrc23* mutant male mice were housed with adult female mice with normal fertility and monitored over two months. The pregnancy and litter size were recorded.

Mouse sperm motility analysis
Motility patterns of the mouse sperm from heterozygous and homozygous *Lrrc23* males were analyzed using computer-assisted sperm analysis (CASA), swimming path analysis, and flagellar waveform analysis as described previously (50, 51). For CASA, motility parameters of over 200 sperm cells were using recorded using Basler acA1300-200μm (Basler AG) equipped in Nikon E200 microscope. Recorded images were analyzed by Sperm Class Analyzer Software (Microoptic). For swimming path analysis, sperm cells were loaded to the HEPES-buffered HTF (H-HTF) with 0.3% methylcellulose (52) and the sperm swimming was recorded. For flagellar waveform analysis, sperm heads were tethered on the fibronectin-coated imaging chamber with H-HTF and the flagellar movement were recorded. Sperm swimming and flagellar movements were recorded using sCMOS camera equipped in Axio observer Z1 microscope (Carl Zeiss). Rendering of the recorded movies were performed by FIJI software (53). See ***SI Appendix, Materials and Methods*** for details.

Sequence alignment, phylogenetic analysis, and protein structure analysis
Alignment of amino acids sequences was carried out by Clustal Omega (https://www.ebi.ac.uk/Tools/msa/clustalo/). Phylogenetic analysis was performed by MEGA7 (54). Protein structures were from PDB (https://www.rcsb.org) or AlphaFold database (55; https://alphafold.ebi.ac.uk/). Images for protein structures were visualized by Mol*3D Viewer at RCSC PDB. See ***SI Appendix, Materials and Methods*** for details.

Tissue and testicular expression analysis
Tissue expression data was from The Human Protein Atlas version 21.0 and Ensembl version 103.38 (https://www.proteinatlas.org/about/download). UMAP images for the single cell expression in testis were from UCSC Cell browser (56; https://cells.ucsc.edu/?ds=testis). See ***SI Appendix, Materials and Methods*** for details.

Transmission electron microscopy
Transmission electron microscopy was performed as previous study (46). Briefly, fixed sperm pellets were placed in agarose and subjected to post-fixation and stained. The samples were dehydrated and placed in molds. The molds were sectioned and collected on the grids. The grids were stained again and imaged using MORADA CCD camera (Olympus) equipped in FEI Tecnai

Biotwin Transmission Electron Microscope (80 KV, FEI, Hillsboro, OR). See ***SI Appendix, Materials and Methods*** for details.

Cryo-electron tomography

For cryo-electron tomography, WT or *Lrrc23*$^{\Delta/\Delta}$ sperm were applied to the grid, which were prepared as previously (20). Prepared grids were plunged into liquid ethane. After initial screening, selected grids were imaged using Titan Krios microscope (300 KV, ThermoFisher Scientific). Tilted series was collected using SerialEM (57) with Volta phase plate (58). Tilted series was used to reconstruct tomograms by AreTomo, Ctffind4 and IMOD (59-61). See ***SI Appendix, Materials and Methods*** for details.

Sub-Tomogram Averaging of 96-nm axonemal doublet repeat

To generate sub-tomogram averaging for 96 nm of axonemal doublet repeat, MTDs were traced manually and each MTD was sampled with 24 nm distance. The repeated sampling particles were aligned, and the Euler angles were extracted using PEET version 1.15.0 (62, 63). Published 96 nm of MTD structure in WT mouse sperm was used as the reference. After preparing the metadata, local 3D refinement with a mask covering 96 nm of MTD was performed using RELION4 (64) and repeats were classified. Resolution was estimated using Fourier shell correlation in RELION4. Images for cryo-ET and sub-tomogram averaging were visualized using IMOD (59) and UCSF Chimerax (65). See ***SI Appendix, Materials and Methods*** for details.

Statistical analysis

Statistical analyses were performed using either Student's t-test or Mann-Whitney U test. Significant differences were considered at $^{*}p \leq 0.05$, $^{**}p<0.01$, and $^{***}p<0.001$.

Acknowledgments

The authors highly appreciate participation of the family members in the study presented here. We also thank Muhammad Umair, Khadim Shah, Imran Ullah, Hammal Khan for their help to visit the family for interviews and participation in clinical assessment, Jong-Nam Oh for preparing samples for WES, Case Porter and Miriam Hill for their help in PCR and Sanger sequencing, the Yale Center for Cellular and Molecular Imaging for assistance in transmission electron microscopy, Dr. Masahito Ikawa from Osaka University for sharing anti-RSPH6A sera. This study was supported by start-up funds from Yale University School of Medicine, National Institute of Child Health and Human Development (R01HD096745), and Grantham Foundation to J-JC; start-up funds from Yale University, National Institute of General Medical Sciences (R35GM142959) to KZ; Pakistan Academy of Sciences (PAS-171) to WA; National Human Genome Research Institute (UM1HG006504) to the Yale Center for Mendelian Genomics. JH was in part supported by Postdoctoral Fellowship from MCI. SN was supported by Pakistan Higher Education Commission International Research Support Initiative Program. JC was in part supported by a Korea University Medical Center Grant. The Genome Sequencing Program Coordinating Center (U24 HG008956) contributed to cross-program scientific initiatives and provided logistical and general study coordination.

References

1. Ishikawa T (2017) Axoneme Structure from Motile Cilia. *Cold Spring Harb Perspect Biol* 9(1).
2. Inaba K (2011) Sperm flagella: comparative and phylogenetic perspectives of protein components. *Mol Hum Reprod* 17(8):524-538.
3. Rao Q*, et al.* (2021) Structures of outer-arm dynein array on microtubule doublet reveal a motor coordination mechanism. *Nat Struct Mol Biol* 28(10):799-810.
4. Kubo S*, et al.* (2021) Remodeling and activation mechanisms of outer arm dyneins revealed by cryo-EM. *EMBO Rep* 22(9):e52911.
5. Smith EF & Yang P (2004) The radial spokes and central apparatus: mechano-chemical transducers that regulate flagellar motility. *Cell Motil Cytoskeleton* 57(1):8-17.
6. Viswanadha R, Sale WS, & Porter ME (2017) Ciliary Motility: Regulation of Axonemal Dynein Motors. *Cold Spring Harb Perspect Biol* 9(8).
7. Witman GB, Plummer J, & Sander G (1978) Chlamydomonas flagellar mutants lacking radial spokes and central tubules. Structure, composition, and function of specific axonemal components. *J Cell Biol* 76(3):729-747.
8. Smith EF & Sale WS (1992) Regulation of dynein-driven microtubule sliding by the radial spokes in flagella. *Science* 257(5076):1557-1559.
9. Abbasi F*, et al.* (2018) RSPH6A is required for sperm flagellum formation and male fertility in mice. *J Cell Sci* 131(19).
10. Liu S*, et al.* (2021) CFAP61 is required for sperm flagellum formation and male fertility in human and mouse. *Development* 148(23).
11. Sironen A, Shoemark A, Patel M, Loebinger MR, & Mitchison HM (2020) Sperm defects in primary ciliary dyskinesia and related causes of male infertility. *Cell Mol Life Sci* 77(11):2029-2048.
12. Zhu X, Liu Y, & Yang P (2017) Radial Spokes-A Snapshot of the Motility Regulation, Assembly, and Evolution of Cilia and Flagella. *Cold Spring Harb Perspect Biol* 9(5).
13. Gui M*, et al.* (2021) Structures of radial spokes and associated complexes important for ciliary motility. *Nat Struct Mol Biol* 28(1):29-37.
14. Yang P*, et al.* (2006) Radial spoke proteins of Chlamydomonas flagella. *J Cell Sci* 119(Pt 6):1165-1174.
15. Bazan R*, et al.* (2021) Ccdc113/Ccdc96 complex, a novel regulator of ciliary beating that connects radial spoke 3 to dynein g and the nexin link. *PLoS Genet* 17(3):e1009388.
16. Ralston KS, Lerner AG, Diener DR, & Hill KL (2006) Flagellar motility contributes to cytokinesis in Trypanosoma brucei and is modulated by an evolutionarily conserved dynein regulatory system. *Eukaryot Cell* 5(4):696-711.
17. Urbanska P*, et al.* (2015) The CSC proteins FAP61 and FAP251 build the basal substructures of radial spoke 3 in cilia. *Mol Biol Cell* 26(8):1463-1475.
18. Pigino G*, et al.* (2011) Cryoelectron tomography of radial spokes in cilia and flagella. *J Cell Biol* 195(4):673-687.
19. Lin J*, et al.* (2014) Cryo-electron tomography reveals ciliary defects underlying human RSPH1 primary ciliary dyskinesia. *Nat Commun* 5:5727.
20. Leung MR*, et al.* (2021) The multi-scale architecture of mammalian sperm flagella and implications for ciliary motility. *EMBO J* 40(7):e107410.

21. Imhof S*, et al.* (2019) Cryo electron tomography with volta phase plate reveals novel structural foundations of the 96-nm axonemal repeat in the pathogen Trypanosoma brucei. *Elife* 8.
22. WHO (2010) *WHO laboratory manual for the examination and processing of human semen* (World Health Organization, Geneva) 5th ed Ed.
23. Curi SM*, et al.* (2003) Asthenozoospermia: analysis of a large population. *Arch Androl* 49(5):343-349.
24. Cavarocchi E, Whitfield M, Saez F, & Toure A (2022) Sperm Ion Transporters and Channels in Human Asthenozoospermia: Genetic Etiology, Lessons from Animal Models, and Clinical Perspectives. *Int J Mol Sci* 23(7).
25. Toure A*, et al.* (2021) The genetic architecture of morphological abnormalities of the sperm tail. *Hum Genet* 140(1):21-42.
26. Martinez G*, et al.* (2020) Biallelic variants in MAATS1 encoding CFAP91, a calmodulin-associated and spoke-associated complex protein, cause severe astheno-teratozoospermia and male infertility. *J Med Genet* 57(10):708-716.
27. Shen Q*, et al.* (2021) Bi-allelic truncating variants in CFAP206 cause male infertility in human and mouse. *Hum Genet* 140(9):1367-1377.
28. Padma P*, et al.* (2003) Identification of a novel leucine-rich repeat protein as a component of flagellar radial spoke in the Ascidian Ciona intestinalis. *Mol Biol Cell* 14(2):774-785.
29. Zhang X*, et al.* (2021) LRRC23 is a conserved component of the radial spoke that is necessary for sperm motility and male fertility in mice. *J Cell Sci* 134(20).
30. Han X, Xie H, Wang Y, & Zhao C (2018) Radial spoke proteins regulate otolith formation during early zebrafish development. *FASEB J* 32(7):3984-3992.
31. Satouh Y & Inaba K (2009) Proteomic characterization of sperm radial spokes identifies a novel spoke protein with an ubiquitin domain. *FEBS Lett* 583(13):2201-2207.
32. Zheng W*, et al.* (2021) Distinct architecture and composition of mouse axonemal radial spoke head revealed by cryo-EM. *Proc Natl Acad Sci U S A* 118(4).
33. Zhao Y*, et al.* (2021) Structural insights into the cause of human RSPH4A primary ciliary dyskinesia. *Mol Biol Cell* 32(12):1202-1209.
34. Lin J, Heuser T, Carbajal-Gonzalez BI, Song K, & Nicastro D (2012) The structural heterogeneity of radial spokes in cilia and flagella is conserved. *Cytoskeleton (Hoboken)* 69(2):88-100.
35. Shamseldin HE*, et al.* (2020) The morbid genome of ciliopathies: an update. *Genet Med* 22(6):1051-1060.
36. Knowles MR*, et al.* (2014) Mutations in RSPH1 cause primary ciliary dyskinesia with a unique clinical and ciliary phenotype. *Am J Respir Crit Care Med* 189(6):707-717.
37. Kott E*, et al.* (2013) Loss-of-function mutations in RSPH1 cause primary ciliary dyskinesia with central-complex and radial-spoke defects. *Am J Hum Genet* 93(3):561-570.
38. Jeanson L*, et al.* (2015) RSPH3 Mutations Cause Primary Ciliary Dyskinesia with Central-Complex Defects and a Near Absence of Radial Spokes. *Am J Hum Genet* 97(1):153-162.
39. Castleman VH*, et al.* (2009) Mutations in radial spoke head protein genes RSPH9 and RSPH4A cause primary ciliary dyskinesia with central-microtubular-pair abnormalities. *Am J Hum Genet* 84(2):197-209.

40. Yin W*, et al.* (2019) Mice with a Deletion of Rsph1 Exhibit a Low Level of Mucociliary Clearance and Develop a Primary Ciliary Dyskinesia Phenotype. *Am J Respir Cell Mol Biol* 61(3):312-321.
41. Yoke H*, et al.* (2020) Rsph4a is essential for the triplet radial spoke head assembly of the mouse motile cilia. *PLoS Genet* 16(3):e1008664.
42. Zou W*, et al.* (2020) Loss of Rsph9 causes neonatal hydrocephalus with abnormal development of motile cilia in mice. *Sci Rep* 10(1):12435.
43. Auguste Y*, et al.* (2018) Loss of Calmodulin- and Radial-Spoke-Associated Complex Protein CFAP251 Leads to Immotile Spermatozoa Lacking Mitochondria and Infertility in Men. *Am J Hum Genet* 103(3):413-420.
44. Kherraf ZE*, et al.* (2018) A Homozygous Ancestral SVA-Insertion-Mediated Deletion in WDR66 Induces Multiple Morphological Abnormalities of the Sperm Flagellum and Male Infertility. *Am J Hum Genet* 103(3):400-412.
45. Ma A*, et al.* (2021) Biallelic Variants in CFAP61 Cause Multiple Morphological Abnormalities of the Flagella and Male Infertility. *Front Cell Dev Biol* 9:803818.
46. Hwang JY*, et al.* (2021) Genetic Defects in DNAH2 Underlie Male Infertility With Multiple Morphological Abnormalities of the Sperm Flagella in Humans and Mice. *Front Cell Dev Biol* 9:662903.
47. McKenna A*, et al.* (2010) The Genome Analysis Toolkit: a MapReduce framework for analyzing next-generation DNA sequencing data. *Genome Res* 20(9):1297-1303.
48. Van der Auwera GA*, et al.* (2013) From FastQ data to high confidence variant calls: the Genome Analysis Toolkit best practices pipeline. *Curr Protoc Bioinformatics* 43:11 10 11-11 10 33.
49. Hwang JY*, et al.* (2019) Dual Sensing of Physiologic pH and Calcium by EFCAB9 Regulates Sperm Motility. *Cell* 177(6):1480-1494 e1419.
50. Hwang JY, Wang H, Lu Y, Ikawa M, & Chung JJ (2022) C2cd6-encoded CatSpertau targets sperm calcium channel to Ca(2+) signaling domains in the flagellar membrane. *Cell Rep* 38(3):110226.
51. Hwang JY, Maziarz J, Wagner GP, & Chung JJ (2021) Molecular Evolution of CatSper in Mammals and Function of Sperm Hyperactivation in Gray Short-Tailed Opossum. *Cells* 10(5).
52. Chung JJ*, et al.* (2017) CatSperzeta regulates the structural continuity of sperm Ca(2+) signaling domains and is required for normal fertility. *Elife* 6.
53. Schindelin J*, et al.* (2012) Fiji: an open-source platform for biological-image analysis. *Nat Methods* 9(7):676-682.
54. Kumar S, Stecher G, & Tamura K (2016) MEGA7: Molecular Evolutionary Genetics Analysis Version 7.0 for Bigger Datasets. *Mol Biol Evol* 33(7):1870-1874.
55. Jumper J*, et al.* (2021) Highly accurate protein structure prediction with AlphaFold. *Nature* 596(7873):583-589.
56. Soraggi S, Riera M, Rajpert-De Meyts E, Schierup MH, & Almstrup K (2021) Evaluating genetic causes of azoospermia: What can we learn from a complex cellular structure and single-cell transcriptomics of the human testis? *Hum Genet* 140(1):183-201.
57. Mastronarde DN (2005) Automated electron microscope tomography using robust prediction of specimen movements. *J Struct Biol* 152(1):36-51.

58. Danev R, Buijsse B, Khoshouei M, Plitzko JM, & Baumeister W (2014) Volta potential phase plate for in-focus phase contrast transmission electron microscopy. *Proc Natl Acad Sci U S A* 111(44):15635-15640.
59. Kremer JR, Mastronarde DN, & McIntosh JR (1996) Computer visualization of three-dimensional image data using IMOD. *J Struct Biol* 116(1):71-76.
60. Rohou A & Grigorieff N (2015) CTFFIND4: Fast and accurate defocus estimation from electron micrographs. *J Struct Biol* 192(2):216-221.
61. Zheng S*, et al.* (2022) AreTomo: An integrated software package for automated marker-free, motion-corrected cryo-electron tomographic alignment and reconstruction. *J Struct Biol X* 6:100068.
62. Heumann JM, Hoenger A, & Mastronarde DN (2011) Clustering and variance maps for cryo-electron tomography using wedge-masked differences. *J Struct Biol* 175(3):288-299.
63. Nicastro D*, et al.* (2006) The molecular architecture of axonemes revealed by cryoelectron tomography. *Science* 313(5789):944-948.
64. Zivanov J*, et al.* (2022) A Bayesian approach to single-particle electron cryo-tomography in RELION-4.0. *bioRxiv*:2022.2002.2028.482229.
65. Goddard TD*, et al.* (2018) UCSF ChimeraX: Meeting modern challenges in visualization and analysis. *Protein Sci* 27(1):14-25.

Figures and Tables

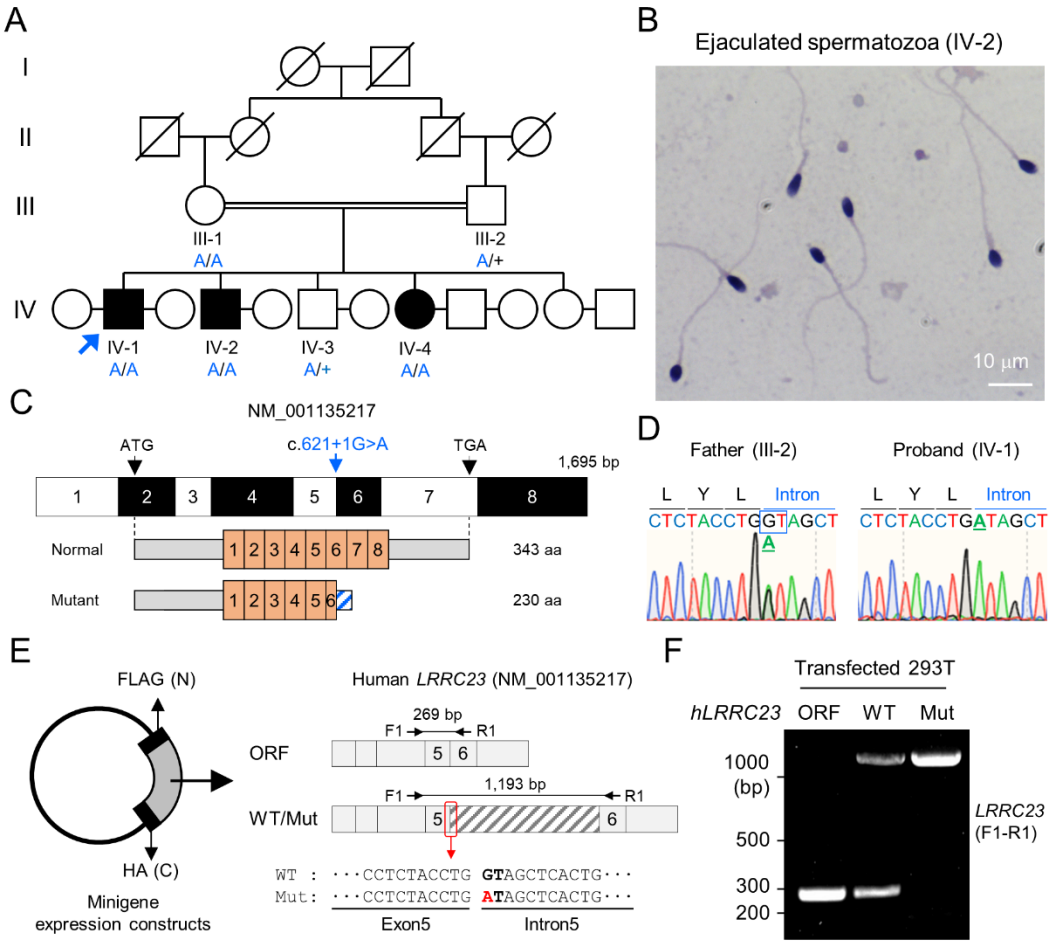

Fig. 1. A bi-allelic splicing donor site variant in *LRRC23* was identified from asthenozoospermia patients. (*A*) A consanguineous pedigree with two infertile males (IV-1 and IV-2). IV-1 was subjected for WES (arrow). Genotypes of the variant (blue) in all attended family members (III-1, III-2, IV-1, IV-2, IV-3, and IV-4) are confirmed by Sanger sequencing. +, wild-type allele. An infertile female sibling (IV-4) is marked in black circle. (*B*) Papanicolaou-stained sperm from the infertile male (IV-2). (*C*) Mapping of the LRRC23 variant. Mutation of G to A at the splicing donor site in the 5th intron is predicted to prevent *LRRC23* mRNA from splicing. (*D*) Sequencing chromatograms presenting the *LRRC23* variant in the infertile male (IV-1) and his father (III-2). The variant is underlined and normal splicing donor site (GT) is boxed. (*E-F*) Minigene assay for testing altered splicing of *LRRC23* by the variant. (*E*) Minigene constructs expressing *LRRC23* ORF containing the 5th intron (sashed) with wild-type (WT) or mutant (Mut, red) splicing donor site were generated. The constructs are tagged with FLAG and HA at N- and C-termini, respectively. (*F*) RT-PCR of the 293T cells transfected with the minigene constructs reveals the 5th intron is not spliced out and retained by the variant. Intron-spanning primers, F1 and R1, are used. Three times biological replicated.

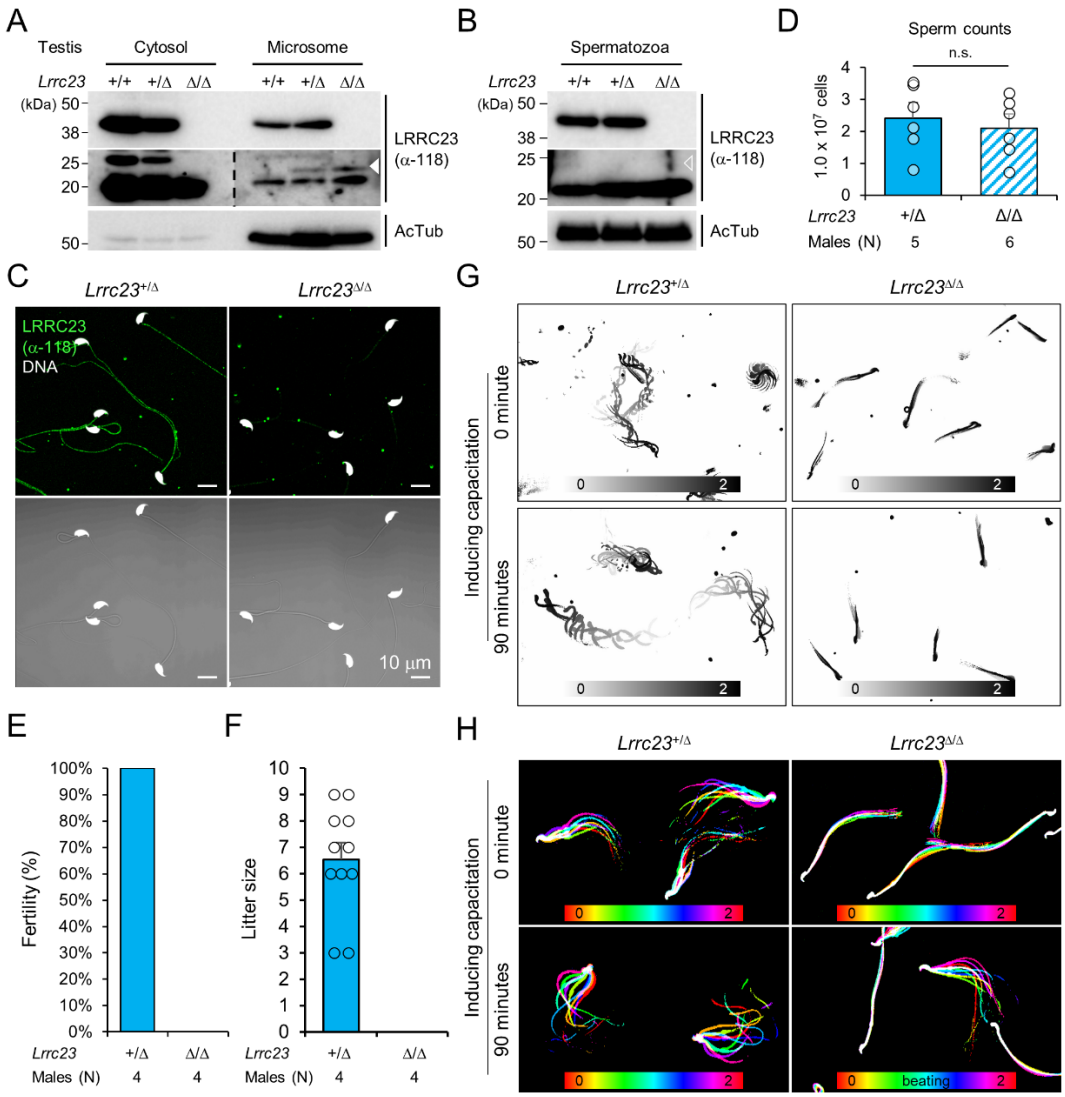

Fig. 2. *Lrrc23* mutant mice mimicking human splice variant phenocopy male infertility and reduced sperm motility. (*A*-*B*) Immunoblotting of LRRC23 in testis (*A*) and epididymal sperm (*B*) from mutant male mice. Truncated LRRC23 (arrowheads) is detected from testis microsome fraction (filled), but not in mature sperm (empty), of heterozygous (+/Δ) and homozygous (Δ/Δ) males. Acetylated tubulin (AcTub) is a loading control. (*C*) Confocal images of immunostained LRRC23 in *Lrrc23*$^{+/\Delta}$ and *Lrrc23*$^{\Delta/\Delta}$ epididymal sperm. Samples from WT were used for positive or negative control of normal or truncated LRRC23 (*A*, *B*, and *C*). (*D*) Epididymal sperm counts. n.s., not significant. (*E*) Pregnancy rate of *Lrrc23*$^{+/\Delta}$ and *Lrrc23*$^{\Delta/\Delta}$ males. (*F*) Number of litters from fertile females mated with *Lrrc23*$^{+/\Delta}$ and *Lrrc23*$^{\Delta/\Delta}$ males. (*G*) Swimming trajectory of *Lrrc23*$^{+/\Delta}$ and *Lrrc23*$^{\Delta/\Delta}$ sperm in viscous media (0.3% methylcellulose). Swimming trajectory for 2 seconds is overlaid. (*H*) Flagellar waveforms of *Lrrc23*$^{+/\Delta}$ and *Lrrc23*$^{\Delta/\Delta}$ sperm before (0 minute) and after (90 minutes) inducing capacitation. Flagellar movements for two beat cycles are overlaid and color coded in time. Circles indicate sperm counts from individual males (*D*) and pup numbers from each litter (*F*). Data represented as mean ± SEM (*D* and *F*). Statistical comparison was perfomed by Mann-whiteny U test (D) or Student's t-test (F). Experiments were repeated three times with biological replications (*A*, *B*, *C*, *G*, and *H*).

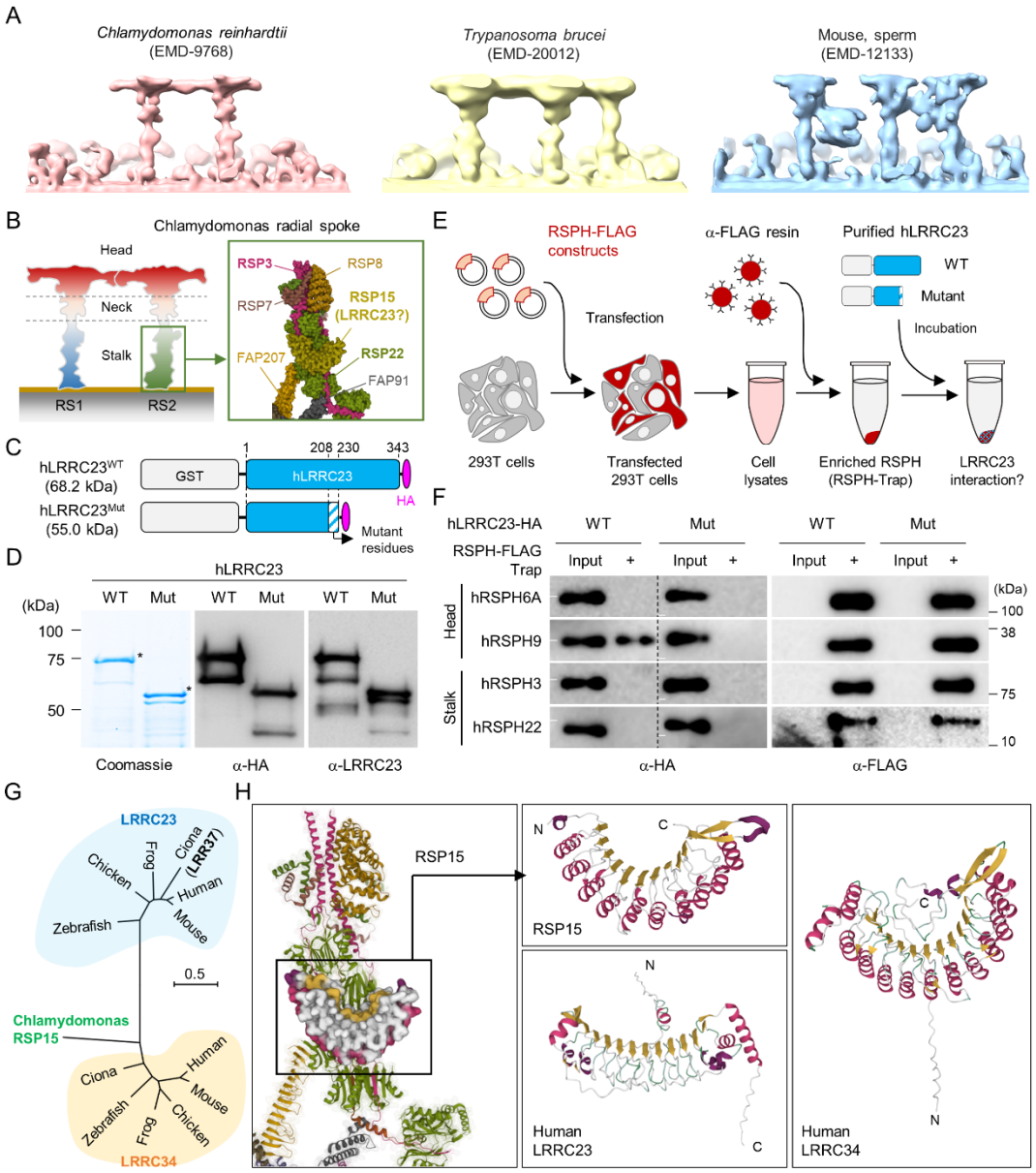

Fig. 3. C-terminal truncation of human LRRC23 by the splicing site mutation prevents its interaction with radial spoke (RS) head. (*A*) Sub-tomogram averaging images of RSs from *Chlamydomonas reinhardtii* (*left*), *Trypanosoma brucei* (*middle*), and mouse sperm (*right*). Original data from Electron Microscopy Data Bank was rendered. (*B*) Structure of RS in *C. reinhardtii*. A schematic cartoon shows the RS1 and 2. The structure of RS2 stalk is shown in inset (PDB Id: 7JRJ). (*C-D*) Purification of normal (hLRRC23^{WT}) and the mutant human LRRC23 (hLRRC23^{Mut}) by the splicing site mutation (c.621+1G>A) in this study. (*C*) Diagrams for the purified recombinant normal and mutant proteins tagged with tagged with GST and HA at N- and C-termini, respectively. (*D*) Purified proteins by Coomassie blue staining (*left*) and immunoblotting with a-HA (*middle*) and a-LRRC23 (*right*). Proteins matched to the predicted size were marked with asterisks. (*E*) A cartoon of the RSPH-trap approach to test LRRC23 interaction with RS proteins. Individual human RS proteins tagged with FLAG (RSPH-FLAG) are expressed in 293T cells and enriched by α-FLAG resin from

cell lysates. The recombinant RSPH proteins were incubated with the purified hLRRC23^{WT} or hLRRC23^{Mut} and subjected to immunoblotting. (*F*) Interaction of hLRRC23 to a RS head component, RSPH9. The purified hLRRC23 were incubated with the RSPH-Trap (RS head, RSPH6A and RSPH9; stalk, RSPH3 and RSPH22) and subjected to immunoblotting. 5% amount of the hLRRC23s used for the trap assay were loaded as inputs. White lines in individual α-HA blot images indicate marker information (75 kDa, *left*; 50 kDa, *right*). Experiments were repeated four times. Purified GST was used for negative control (***SI Appendix*, Fig. S4*B***). (*G*) A phylogenetic tree constructed by Maximum-likelihood analysis of the protein sequences of the *C. reinhardtii* RSP15 and the orthologs of LRRC23 and LRRC34. LRR37, the first LRRC23 ortholog identified in *Ciona intestinalis* is marked in bold. (*H*) Comparison of the reported RSP15 from *C. reinhardtii* and the predicted structure of LRRC23 and LRRC34 from human. Atomic structure of the *C. reinhardtii* RS2 containing RSP15 are represented by ribbon (RS2) and surface (RSP15) diagram (*left*, PDB Id: 7JU4). Ribbon diagrams of *C. reinhardtii* RSP15 and AlphaFold-predicted human LRRC23 (*middle*) and LRRC34 (*right*) are shown for structural comparison. Secondary structures are color-coded. Different from *C. reinhardtii* RSP15 and LRRC34, LRRC23 does not display repeated α-helix (magenta) between β-sheets (gold).

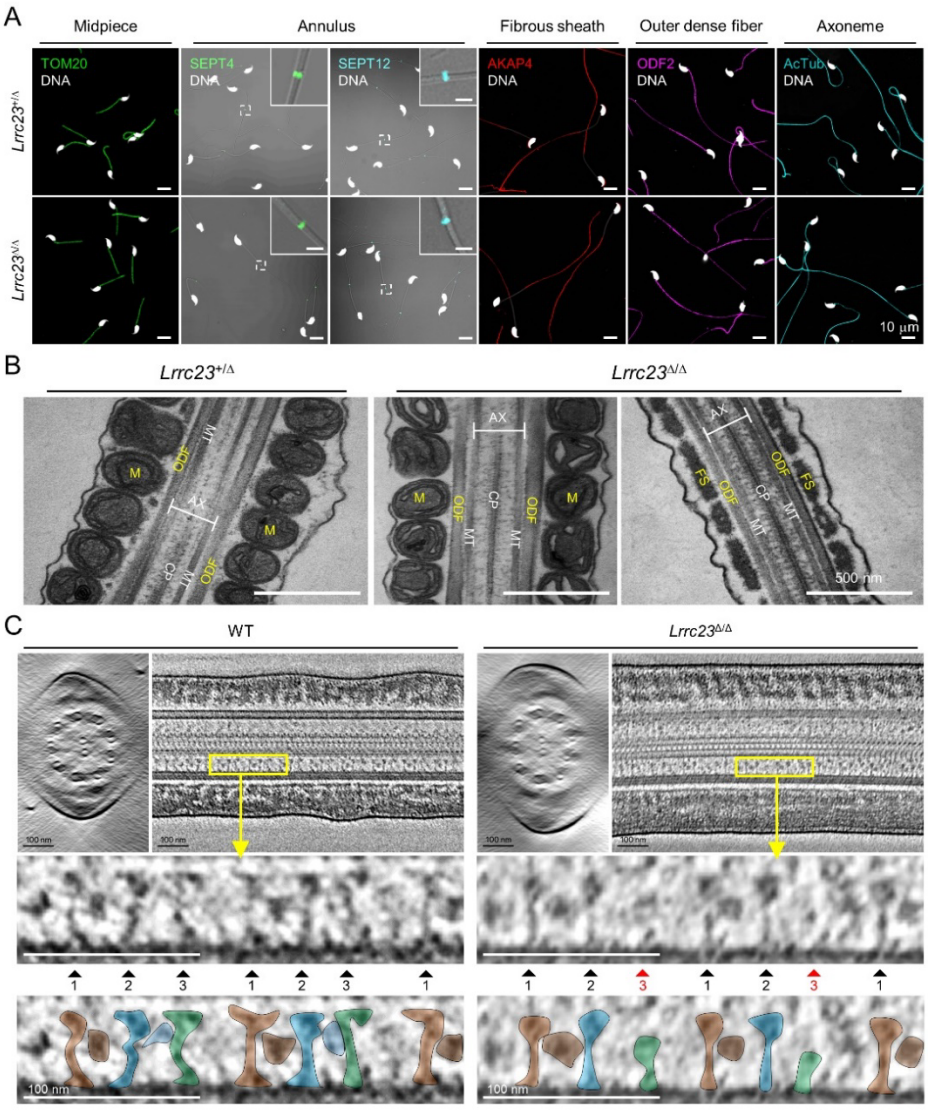

Fig. 4. LRRC23 mutation disrupts the third radial spoke (RS) in sperm flagellum. (*A*) Immunostaining of flagellar proteins in different compartments. Shown are midpiece (TOM20), annulus (SEPT4 and SEPT12), fibrous sheath (AKAP4), outer dense fiber (ODF2), and axoneme (acetylated tubulin, AcTub) in *Lrrc23*$^{+/\Delta}$ (*top*) and *Lrrc23*$^{\Delta/\Delta}$ (*bottom*) sperm. Magnified insets are represented for annulus proteins (scale bars in insets = 2μm). Fluorescence and corresponding DIC images are merged. Sperm heads were counter stained with Hoechst. Experiments were performed with three biological replications. (B) Transmission electron microscopy images of *Lrrc23*$^{+/\Delta}$ (*left*) and *Lrrc23*$^{\Delta/\Delta}$ (*right*) sperm. Shown are longitudinal section of sperm flagella. M, mitochondria; ODF, outer dense fiber; AX, axoneme; CP, central pair; MT, microtubule; FS, fibrous sheath. (*C*) Cryo-electron tomography (cryo-ET) of WT and *Lrrc23*$^{\Delta/\Delta}$ sperm flagella. Shown are representative tomographic slices from WT (*left*) and *Lrrc23*$^{\Delta/\Delta}$ sperm (*right*). The 9+2 axonemal structure are shown in both WT and *Lrrc23*$^{\Delta/\Delta}$ in cross-sectional view (*left*). Axonemal structures are shown with proximal side of the flagellum on the left in longitudinal view (*right*). Magnified insets (*bottom*) reveal that RS1, 2, and 3 are shown in WT sperm (*left*, filled arrowheads) but RS3, especially head part, is not clearly visible (*right*, red arrowheads) in *Lrrc23*$^{\Delta/\Delta}$ sperm. *Lrrc23*$^{+/\Delta}$ (*A* and *B*) or WT (*C*) sperm were used for positive control.

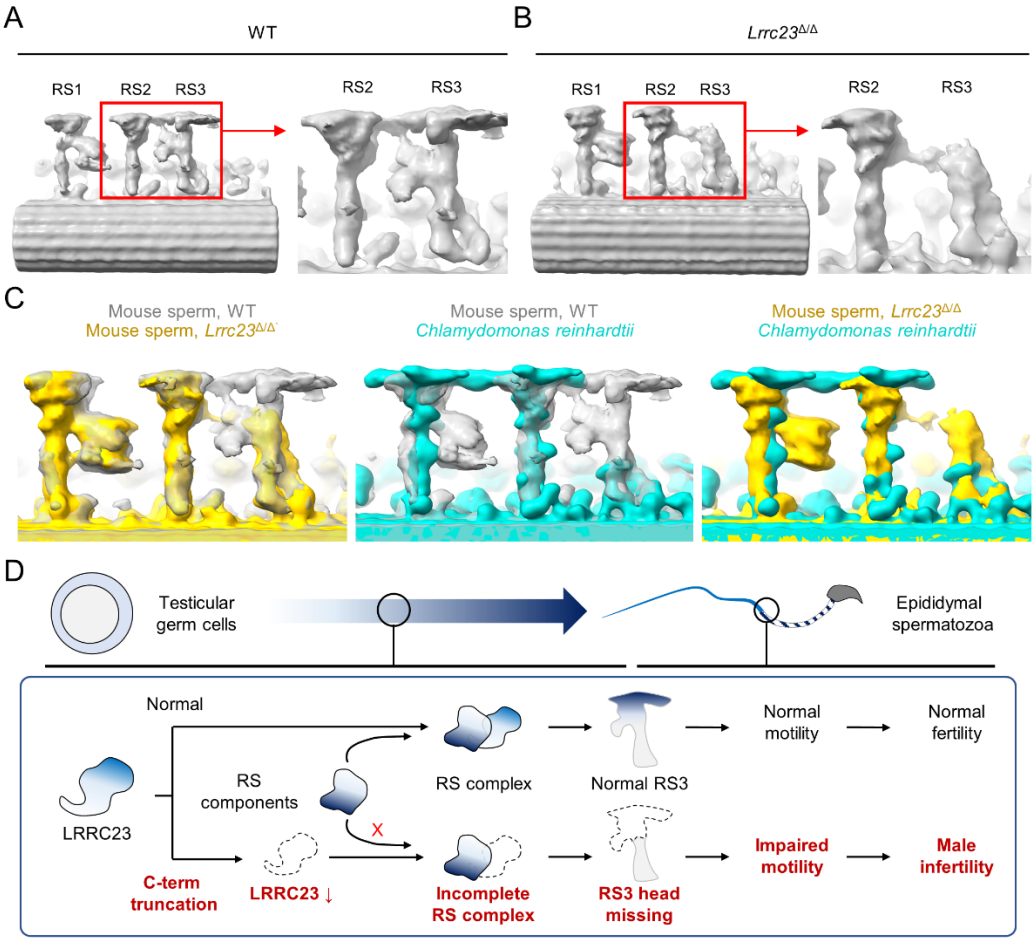

Fig. 5. Head of the third radial spoke is absent in *Lrrc23*$^{\Delta/\Delta}$ sperm flagella. (*A-B*) Sub-tomogram averaging (STA) to analyze structural defects at radial spoke (RS) of WT (*A*) and *Lrrc23*$^{\Delta/\Delta}$ sperm (*B*). Shown are STA images resulted from 96-nm doublet repeats from WT and *Lrrc23*$^{\Delta/\Delta}$ sperm. RS2 and 3 are magnified and density to represent RS3 head and the bridge between RS2 and RS3 (red circle) is missed in *Lrrc23*$^{\Delta/\Delta}$ sperm specifically. (*C*) Overwrapped STA images from 96 nm-doublet repeats from WT (gray) and *Lrrc23*$^{\Delta/\Delta}$ (gold) sperm, and *Chlamydomonas reinhardtii* (cyan). (*D*) A proposed model of impaired sperm motility and male infertility by the LRRC23 loss of function.